Evaluation of the CAMEL Land Surface Emissivity Model over the Taklimakan Desert using Field Observations

Yufen Ma[1], Wei Han[2], Zhenglong Li[3], Ali Mamtimin[1], Eva E. Borbas[4], and Yongqiang Liu[5]

[1]Institute of Desert Meteorology,CMA
[2]China Meteorological Administration
[3]Cooperative Institute for Meteorological Satellite Studies (CIMSS), University of Wisconsin-Madison
[4]University of Wisconsin - Madison
[5]College of Resource and Environmental Sciences, Xinjiang University

November 24, 2022

Abstract

A set of LSE observations from field experiments were conducted on 16-18 Oct 2013 along a south/north desert road in the Taklimakan Desert (TD), China. The observed LSEs (EOBS) are thus used in this study as the reference to evaluate the quality of Combined ASTER MODIS Emissivity over Land (CAMEL). Analysis of these data shows four main results. Firstly, the CAMEL appears to capture the spatial variations of LSE from the oasis to the hinterland of TD well, especially in the quartz reststrahlen band 8.1 mm, 8.6 mm and 9.1 mm. From site 1 at the south edge of the TD to site 10 at the north edge, the EOBS and the corresponding CAMEL in the quartz reststrahlen band firstly decrease and reach their minimum around sites 4-6 at the hinterland of the TD. Then the LSE increases gradually and finally gets their maximum at site 10 with clay ground surface, which is higher at the edges of the desert and lower in the center. Second, the CAMEL at 8.3 mm has a Zonal distribution characteristic of northeast-southwest strike. Third, the unrealistic variation of original EOBS can be filtered out with useful signals remaining by the first 6 principal components from PCA upon the laboratory measured hyperspectral emissivity spectra (ELAB). Fourth, the CAMEL correlates well with the measured LSE at the ten observation sites, with the EOBS slightly smaller than CAMEL in general.

Hosted file

Yufen Ma, Wei Han, Zhenglong Li, E. Eva Borbas, Ali Mamtimin, Yongqiang Liu

1 Institute of Desert Meteorology, China Meteorological Administration, Urumqi 830002, China; mayf@idm.cn (Y.M.); ali@idm.cn (A.M.)

2 National Observation and Research Station of Desert Meteorology, Taklimakan Desert of Xinjiang, Urumqi 830002, China

3 Taklimakan Desert Meteorology Field Experiment Station of China Meteorological Administration, Urumqi 830002, China

4 China meteorological administration Earth system Modeling and prediction Centre (CEMC), Beijing 10081, China; hanwei@cma.gov.cn (W.H.)

5 The State Key Laboratory of Severe Weather (LaSW), China Meteorological Administration, Beijing 10081, China

6 Cooperative Institute for Meteorological Satellite Studies, University of Wisconsin-Madison, WI 53706, U.S.A.; zhenglong.li@ssec.wisc.edu (Z.L.); evab@ssec.wisc.edu (E.B.)

7 College of Resource and Environmental Sciences, Xinjiang University, Urumqi, China; liuyq@xju.edu.cn (Y.L.)

* Correspondence: hanwei@cma.gov.cn; Tel.: +86-13811971993

[1]***Abstract*—Infrared (IR) land surface emissivity (LSE) plays an important role in numerical weather prediction (NWP) models through the satellite radiances assimilation. However, due to the large uncertainties in LSE over the desert, many land-surface sensitive channels of satellite IR sensors are not assimilated. This calls for further assessments of the satellite retrieved LSE quality in these desert regions. A set of LSE observations from field experiments were conducted on 16-18 Oct 2013 along a south/north desert road in the Taklimakan Desert (TD), China. The observed LSEs (EOBS) are thus used in this study as the reference to evaluate the quality of Combined ASTER MODIS Emissivity over Land (CAMEL). Analysis of these data shows four main results. Firstly, the CAMEL appears to capture the spatial variations of LSE from the oasis to the hinterland of TD well, especially in the quartz reststrahlen band 8.1 m, 8.6 m and 9.1 m. From site 1 at the south edge of the TD to site 10 at the north edge, the EOBS and the corresponding CAMEL in the quartz reststrahlen band firstly decrease and reach their minimum around sites 4-6 at the hinterland of the TD. Then the LSE increases gradually and finally gets their maximum at site 10 with clay ground surface, which is higher at the edges of the desert and lower in the center. For the four sets of LSE with wavelengths 10.6 m, 10.8 m 11.3 m, and 12.1 m respectively, the LSE remains almost the same at all 10 observing sites.**

[1]

Second, the CAMEL at 8.3 m has a Zonal distribution characteristic of northeast-southwest strike; such an artifact might be caused by ASTER LSE through the merging process to create CAMEL. Third, the unrealistic variation of original EOBS can be filtered out with useful signals remaining by the first 6 principal components from PCA upon the laboratory measured hyperspectral emissivity spectra (ELAB). Fourth, the CAMEL correlates well with the measured LSE at the ten observation sites, with the EOBS slightly smaller than CAMEL in general. The quartz reststrahlen band around 9.1 m has the most significant discrepancy, possibly due to the diurnal variations associated with soil moisture change. In addition, the variations of the EOBS and CAMEL between different wavelength bands at the last two observing sites with clay ground surfaces are smaller than that from sheer desert sites.

Key words: **Infrared land surface emissivity; the Taklimakan desert; CAMEL; field observation; laboratory measurement**

1. INTRODUCTION

The TD in China is the second largest desert in the world, which plays an important role in regional climate change and energy exchange between the land surface and atmosphere. In recent years, extremely heavy precipitation events in and around TD become more frequent than ever before [1]. Due to the special geography and land-surface type as well as soil texture, local severe storms (LSSs) with tens of millimeters of precipitation in several hours may induce mountain torrent or debris flow on the hillside of Mt. Tianshan and Mt. Kulun around TD, causing serious casualties and economic losses [2]. Accurate and timely weather forecasts are thus rather critical in this region. Numerical Weather Prediction (NWP) modeling with high temporal and spatial resolution can be a useful tool to achieve this goal [3].

The accuracy of NWP models highly depends on the initial condition [4]. The assimilation of observations with high quality and proper spatial distribution density is essential. However, only seven conventional synoptic stations and three synoptic radars are located at oasis regions around the TD without any meteorological stations in the hinterland of the grand desert regions, an area of 330,000 square kilometers [5]. That is far from enough to provide accurate initial conditions. Satellite data can and should be used to fill the data gap in this region [6].

With the improvement of instrumentation and data assimilation technologies, satellite data has been playing an increasingly important role in improving the NWP [7]. At present, the number of satellite data used by operational centers in Europe and the United States has reached more than 90% [8]. The use of satellite data has improved the lead time of prediction in the southern hemisphere for more than two days and nearly one day in the northern hemisphere

[7].

Even with the overwhelming use of satellite measurements by NWP centers [8], the forecast of when and where LSSs are going to form is still challenging. Part of the reason is due to the lack of accurate initial conditions of the boundary layer and the land surface [9, 10]. In recent years, progress has been made on assimilating IR surface channel radiances [11, 12]. However, most NWP centers are still not assimilating those radiances, partly due to the complexity of the land surface.

As two important characteristics of the land surface, land surface temperature (LST) and land surface emissivity (LSE), are difficult to estimate accurately, resulting in limited use of surface channels in assimilation system [13]. The LST and LSE are two important terms in the radiative transfer equation (RTE). They together characterize how large the surface emission is. This term has a significant contribution to the RTE [14]. In addition, the LSE also affects how large the atmospheric downwelling radiances are reflected back by the surface. While this term usually has a minor contribution in the RTE, it is not negligible, especially when LSE is substantially smaller than 1, i.e. in the desert [15]. Accurately simulating the surface emission and the surface reflection with accurate LST and LSE will make it possible to successfully assimilate the surface and the water vapor channel radiances in dry conditions, i.e. winter or high terrains [16]. It is possible to simultaneously analyze the LSE and LST in the assimilation system in addition to the temperature and moisture profiles. However, the addition of the unknowns (LSE and LST) and the strong correlations between them add significant difficulties in the inverse problem [13].

LSE is one of the inherent physical properties of surface materials [17]. It is not only related to the composition of surface soil materials but also related to surface roughness and soil moisture [18-21]. LSE vary with surface types, making it difficult to accurately characterize [22-25]. Besides the surface channel radiance assimilation, LSE is an important input parameter in many other applications related to the surface. In LST inversion, for a typical LST of 300 K, an LSE error of 0.01 will lead to an LST inversion error of about 1 K. Accurate LSE is also important for climate models. For example, a broadband surface emissivity error of 0.1 will result in errors of up to 7 $W \cdot m{-}2$ in the upward long-wave radiation estimates, which is much larger than the surface radiative forcing (~2–3 $W \cdot m{-}2$) due to an increase in greenhouse gases [15].

Since the launch of the National Aeronautics and Space Administration (NASA) ‘s Earth Observing System (EOS) Terra and Aqua satellites and the European Meteorological Satellite (EUMETSAT) Meteorological Operational A (MetOp-A) satellite, more realistic representations of the spectral IR emissivity spectrum have been developed. For example, the NASA Moderate Resolution Imaging Spectroradiometer (MODIS) MOD11C3 monthly land surface temperature and emissivity products [26] on 5km spatial resolution using the day/night algorithm have been well evaluated. But the MODIS MOD11 products are only available at selected MODIS spectral bands. To expand the spectral coverage, and more importantly, the spectral resolution, a MODIS-based Baseline Fit Emissivity database (BFEMIS) was developed at the University of Wisconsin-Madison using laboratory measurements to fill up the spectral gaps [27]. This dataset has been extensively used in research and operational applications. It has been incorporated into the RTTOV radiative transfer model [(Borbas and Ruston 2011; Saunders et al. 1999). A Global Emissivity Dataset from Advanced Spaceborne Thermal Emission and Reflection Radiometer (ASTER GED) was also created at the Jet Propulsion Laboratory (JPL) to provide thermal emission emissivity measurements at 100-meter resolution [28].

Recently, the ASTER GED V4 was incorporated to augment the spectral coverage of the UW BFEMIS database in critical wavelengths and to stabilize the time dependence of the operational MODIS MOD11 emissivity product. As a result, the new dataset called the Combined ASTER MODIS Emissivity over Land (CAMEL) dataset [29], has been developed under the NASA Making Earth System Data Records for Use in Research (MEaSUREs) program. As the first step toward the assimilation of radiances in TD, the CAMEL LSE is compared with field measurements at selected locations in the TD desert in this paper.

2. MATERIALS AND METHODS

2.1 LSE observations from field experiments

LSE observations over 10 locations in the TD from field experiments conducted on 16-18 Oct 2013 [30] are used as the reference to evaluate CAMEL. Using a portable Fourier transform infrared spectrometer (FTIR) with radiances of a blackbody in cold and warm conditions as well as a gold diffuse plate calibrated (Fig. A1 in appendix A), the LSE are measured in the spectrum of 8-14 m from 10 different sites along a south/north desert road every 50 km [30]. Generally, more than three sets of EOBS has been obtained by land-surface emissivity spectrum measurements, with the inefficient observations kicked out. To get a more preferable EOBS with higher quality, the fine and dry weather conditions were selected to conduct the field observation experiments, since the cloudy weather would increase the observation error and further lower down the measurement precision. To rectify the emissivity, the 102F spectrometer has to be calibrated by blackbody for one time every 10-20 minutes. Meanwhile, the cold blackbody temperature are required to be set 10 ℃ lower than surrounding temperature, and 10 ℃ higher than the land surface temperature at the same location. Once the proper blackbody temperature has been initialized, the actual temperature of the cold and hot blackbody needs to be measured and saved. The precision of blackbody emissivity could reach up to 0.994-0.998$\pm$0.002, and the temperature precision for $\pm$0.1 ℃, and the error caused by blackbody is minor than 0.004 with such a setup. The temperature fluctuation range of interferometer is within 0.1 ℃, and the error of the blackbody itself is smaller than 0.002 [31]. To lower down the equipment noise signal interference, the scanning spectrum overlap count is usually set to 10, and the mean of the overlap times are finally adopted by the interferometer [30].

In the field measurement process, three steps has been followed to minimize the observing erros and obtain EOBS with possible higher accuracy. First, measurement of radiaiton of the cold blackbody, the hot blackbody and the diffuse gold plate. Second, measurement of land-sureface emissivity. Third, reconduction of the first step. The emissivity of diffuse gold plate (5×5 inch, developed by Labsphere, a company from the United States) is 0.04 approximately, and the factory calibration value should be used in actual operation. To avoid the disadvantagous affect from the weather-condition variations upon the emissivity of the instument itself and its further impact on the precision of EOBS in the field sampling process, all these listed 3 steps should be completed as swift as possible, and the time limits of a single sampling process are thus refined in 10 minites. The purpose of step 1 and step 3 is to evalute the impact of variation of surounding factors upon the land-surface emissivity spectrum, and lower down the error introduced from the meansurement process. The skin temperature of the diffuse gold plate are directly measured by the thermoelectric coupled thermometer (Model 51, Fluke, a company of USA), the average value of each 5 observations are use as usual.

A credible measurement method of land surface temperature (LST) are critical for calibration of emissivity. Althogh the LST could be meausured directly by the thermoelectric coupled thermometer, the land surface radiation temperature can not be well reflected. Fortunately, a module has been included in the software of th 102F spectrometer, this modle are capable of fitting the land-surface radiation spectrum from blackbody radiation spectrum by Planck function, and further calculated out the land-surface radiation temperature, which is thus called blackbody fitting for short. For the desert ground surface, Korb et al suggested that, the maximum emissivity of fitting wavelength band in 7.45 to 7.65 m should be 0.995. The land-surface radiation temeprature obtained by black fitting method in this wavelengh band are quiet credible, with its calculated LSE error smaller than 0.008. Therefore, the fitted land-sureface radiation temperature are also used in the calculation of emissivity specture at all wavelengths [31, 32]. The field oberation experiments also proved that, the blackbody fitting methodology are efficient and facilate in obtaining the land-surface radiation temperature as well as calculation of the infrared LSE with wavelengh range 8-14 m in TD.

$$e_s(l) = \frac{[L_{\mathrm{uwr}}(l) - L_{\mathrm{dwr}}(l)]}{[B[l, T_s] - L_{\mathrm{dwr}}(l)]} \tag{1}$$

where $e_s(l)$ is the surface emissivity of the sample as a function of wavelength (l); $L_s(l)$ is the calibrated radiance of the sample; $L_{\mathrm{dwr}}(l)$ is the calibrated radiance of the downwelling radiance; and $B\,[l, T_s]$ is a Planck function at the sample temperature. The exact locations and surface type category of the ten sites are detailed in Table A1 and Fig. 1. Most of the sites are in the inner domain of TD, while sites 1 and 10 are close to or at the oasis.

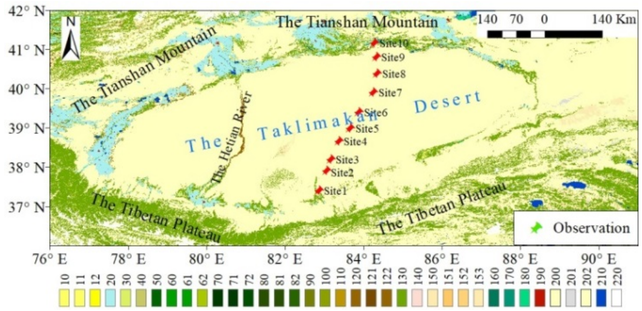

Fig. 1. Locations of field experiments (Table 1) and the land type description in and around TD. Different surface label indexes represent different surface types (Table A1)

TABLE I

ALTITUDE, LOCAL SOLAR TIME, AND LAND CATEGORY OF THE TEN OBSERVATION SITES

EOBS sites	Altitude (m)	LST	Land category
Site 1	1334	2013/10/16 14:04	sand
Site 2	1252	2013/10/16 10:08	sand
Site 3	1182	2013/10/16 15:44	sand
Site 4	1115	2013/10/16 16:53	sand
Site 5	1088	2013/10/17 09:19	sand
Site 6	1028	2013/10/17 15:36	sand
Site 7	967	2013/10/18 09:45	sand
Site 8	920	2013/10/18 11:05	sand
Site 9	917	2013/10/18 12:59	silt soil
Site 10	912	2013/10/18 16:43	clay

2.2 CAMEL ESDR database

The version 2 CAMEL Earth System Data Record (ESDR) from October 2013 is used, which is a monthly global LSE database at 5km resolution (Borbas et al., 2018). It is available at 13 hinge points from 3.6-14.3 m. Out of the 13 hinge points, only seven are overlapped with the spectral coverage of EOBS. The wavelengths of these seven hinge points are 8.3 m, 8.6 m, 9.1 m, 10.6 m, 10.8 m 11.3 m, and 12.1 m, respectively.

3. Comparison between CAMEL and EOBS in TD

3.1 Noise filtering of EOBS

The LSE observations (EOBS) from the field experiments are shown in Fig. 2, which are the original observations without any statistical operations including averaging. The wavelength of EOBS ranges from 7.89 m to 14.10 m, with 416 channels [30]. The general pattern is consistent with the laboratory measured desert sand LSE spectrum; the LSE decreases with the increase of wavelength around 8 m, reaching the minimum around 9.3 m, and then increases until the maximum wavelength. Such a pattern is obvious for the first 8 sites while much more subtle for the last two sites, especially for site 10 with clay ground surface.

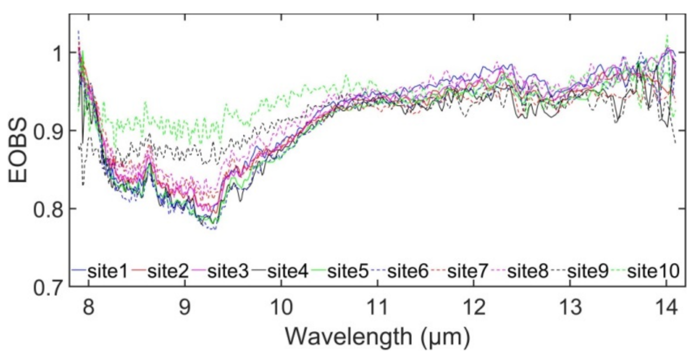

Fig. 2. The land surface emissivity measurements from the field experiments at 10 observation sites in TD

However, the measured LSE appears to be quite noisy, especially in the longwave region, where LSE is expected to be spectrally smoother. The maximum value of EOBS is even larger than 1.0 for some sites. Such phenomenon is likely caused by excessive noise in the observing process. To filter out the noise in EOBS, the Principal Components Analysis (PCA) noise filtering method is used [33].

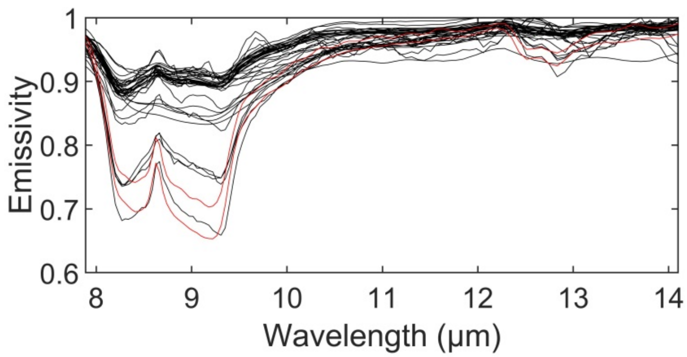

Fig. 3. 42 selected laboratory measured sandy samples from 123 ELAB hyperspectral emissivity spectra. The two red lines show two typical sandy samples

The noise filtering is performed in four steps. In the first step, the 42 sandy hyperspectral emissivity spectra at 416 wavelengths in the infrared region from 7.8942 m to 14.0964 m. are selected from the 123 laboratory emissivity spectra (wavenumber resolution between 2-4 cm^{-1}) used in the UW BFEMIS database (Table B2). The selection method of the 123-laboratory set is described in Section 1 of Seemann et al, 2008. They show a similar spectral pattern with EOBS, which first lowers down, reaching their minimum between 8 m and 9 m, and then increases until 11 m. After 11 m, the spectral variations are subtle (Fig. 3). In the second step, the 42 laboratory-measured emissivity spectra are used to generate Eigenvectors. The Eigenvectors are ranked by their importance, i.e. the most important Eigenvector or the one explaining the most variances is the first Eigenvector. The least important ones are last Eigenvectors. And they usually explain the noise information. Fig. 4 shows the first 4 Eigenvectors can explain 99.1% of the variances. And the first 8 can explain 99.8%. In the second step, the Eigenvectors are used to decompose the EOBS spectra. Each EOBS spectrum can be decomposed to get the coefficient for each Eigenvector or the Eigenvalue. In the last step to perform noise filtering, one needs to use a certain number of PCs to re-construct the EOBS. Since last Eigenvectors for noise information are not used, the reconstructed EOBS is noise filtered.

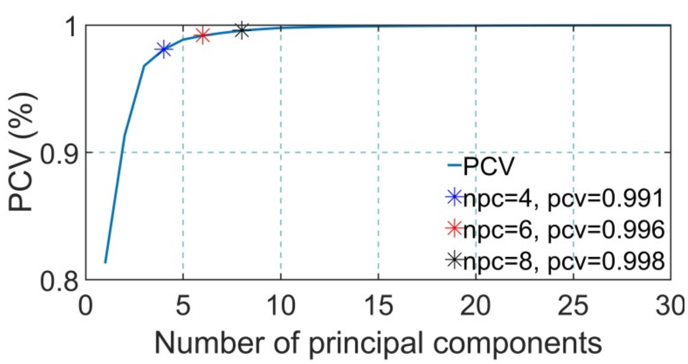

Fig. 4. Percentage cumulative variance (PCV) of the 123 selected laboratory measurement sets as a function of the number of principal components (NPC). The legend contains the corresponding PCV values.

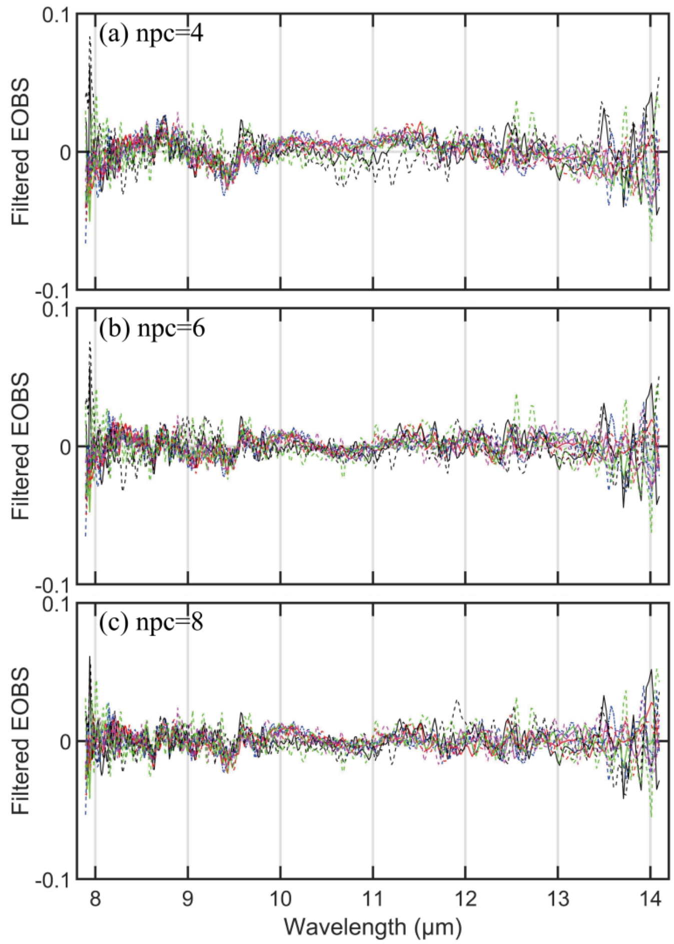

Fig. 5. Bias (after minus before) of the hyperspectral LSE observation at the ten sites in TD before and after filtering with first 4 PCs (a) and 6 PCs (b) as well as 8 PCs (c)

Fig. 5 shows the residual of the 10 EOBS spectra (the original minus the reconstructed spectra) using different number of PCs. When the proper number of Eigenvectors is used, the residual should be dominated by noise, thus appearing random. Too few Eigenvectors result in loss of signal and too many result in less noise filtered. As shown in Fig. 5a, when the first 4 PCs are used to filter the EOBS, the maximum residual of the 10 EOBS spectra reaches up to 0.0834 at 7.9372 m over site 9. The residual becomes 0.0756 at 7.9392 m over site 9 with the first 6 PCs, and 0.0614 at 7.9392 m over site 4 with the first 8 PCs.

All those maximum residuals with different PC numbers occurred at wavelength between 7.93 m and 7.94 m, with 2 of the 3 maximum values appear over site 9 with clay ground surface soil category. In addition, majority of all the maximum residuals for the ten sites appear at wavelength smaller than 9 m, and the rest maximum values appear at wavelength larger than 13 m, such a distribution feature has also been present in Fig. 5.

As shown in Table , the correlation coefficient between the original EOBS and the mean of the two sandy samples of ELAB is smaller than that after the filtering with the first 6 PCs of ELAB. The mean correlation coefficient of the 10 sites is increased from 0.910 to 0.951, 0.957, and 0.948 with the number of principle components of ELABS equal to 4, 6 and 8, respectively, indicating that the filtering of the EOBS makes the LSE spectra closer to sandy spectra, and the maximum number of PCs allowed is thus finally determined to be 6. This is consistent with Borbas et al. (2018) where the first 6 PCs are also used to derive high spectral resolution emissivity.

TABLE

COEFFICIENCY BETWEEN ELAB OF 42 SELECTED LABORATORY MEASURED SANDY SAMPLES AND EOBS BEFORE (ORIGINAL) AND AFTER (FILTERED) NOISE FILTERING WITH FIRST 6 PCS OF ELAB USED

Sites	Original	Filtered		
		PC4	PC6	PC8
Site1	0.947	0.96	0.968	0.96
Site2	0.926	0.94	0.947	0.938
Site3	0.924	0.945	0.952	0.943
Site4	0.926	0.951	0.952	0.95
Site5	0.929	0.945	0.949	0.943
Site6	0.927	0.948	0.953	0.946
Site7	0.892	0.906	0.912	0.902
Site8	0.942	0.964	0.97	0.963
Site9	0.836	0.959	0.969	0.94
Site10	0.846	0.996	0.998	0.992
Mean value	0.91	0.951	0.957	0.948

After the noise filtering, the unrealistic spectral variations in the original EOBS from the ten sites in TD are not obvious any more, and the unrealistic noise with wavelength shorter than 8 m and larger than 14 m has been successfully filtered out. For example, the original maximum EOBS value of 1.0279 at site 6 has been adjusted to 0.9676 after the filtering process. The filtered LSE appears to have more realistic spectra (Fig. 6) when compared with the spectra of the two sandy samples from ELAB (solid red lines in Fig. 3).

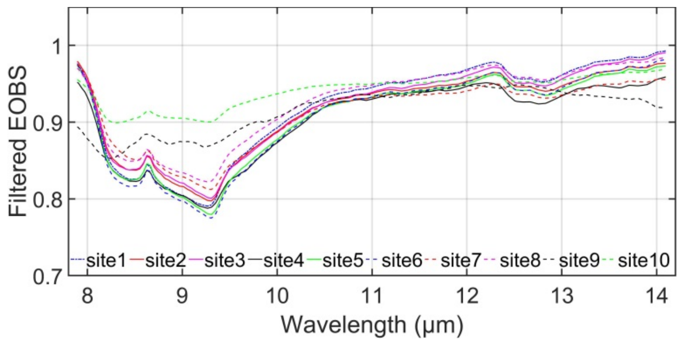

Fig. 6. The 10 new noise filtered spectra of EOBS with first 6 PCs of ELAB used

3.2 CAMEL in TD

The CAMEL imagery at 8.3 m, 8.6 m, and 9.1 m are shown in Fig. 7. For these three wavelengths, TD has LSE much smaller than surrounding areas. The minimum values are 0.80 to 0.82. The LSE spatial variations in the TD match with the surface types well, as shown in Fig. 1. For example, the regions that the Hetian River runs through, from (37°N, 80°E) to (40°N, 80.5°E), have LSE larger than other areas on all three imagery. To the east of the Hetian River, a second river, the Keriya River, from (37°N, 81.5°E) to (38.5°N, 82°E), is also visible on the 8.6 m imagery. The river ends at the oasis Daliyabuyi where LSE is also larger than the surrounding desert. Along the east half of the south boundary of the TD, a belt with LSE significantly larger than desert sands runs from (37°N, 82.5°E) to (39°N, 87.5°E). This belt is also seen in Fig. 1. In addition, many other surface features are recognizable on the CAMEL imagery, such as water reservoirs and snow-covered mountain tops. These results indicate that the CAMEL LSE database is able to capture the spatial variations in the region and correctly identify regions with large LSE from low.

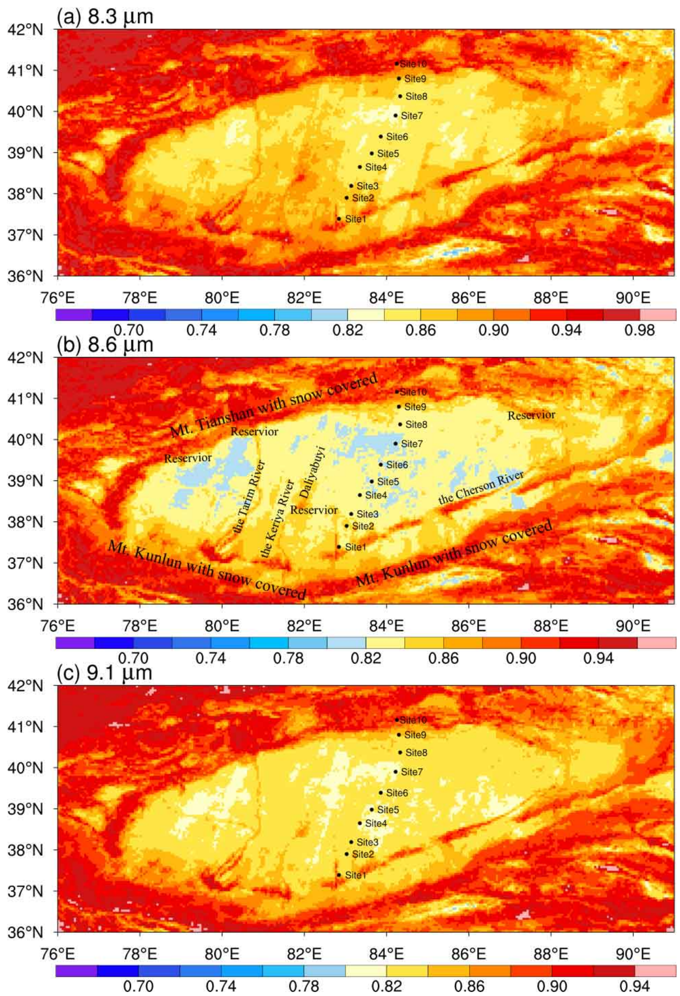

Fig. 7. The CAMEL LSE at 8.3 m (a), 8.6 m (b) and 9.1 m (c) in TD for Oct 2013

It should also be noted that the CAMEL appears to have some artifacts for 8.3 m with strips from north northeast by norh (NNE) to south southwest (SSW) (Fig. 7(a)). Such artifacts are likely due to the lack of temporal resolution from ASTER. Li et al. (2012) showed a wave-like diurnal variation of LSE in the quartz reststrahlen band. Such temporal variations in LSE are due to soil moisture diurnal variations. The ASTER has a narrow swath of 160 km and a low revisit rate of 16 days. The lack of revisit rate makes it difficult to smooth out the temporal difference and leads to artifacts like those shown in Fig. 7 a in the monthly CAMEL product. The lack of temporal variation in the monthly CAMEL may pose some difficulties in its applications. This is likely more important around local noon time due to strong evaporation from the top-level soil with high LST.

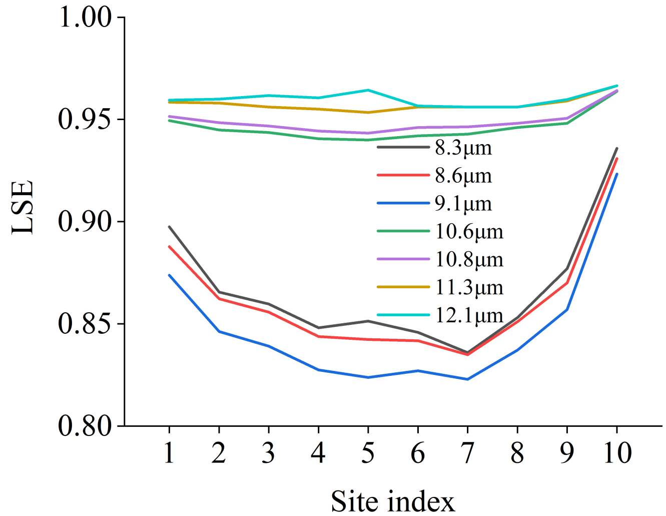

Fig. 8. The CAMEL LSE at the seven hinge points for the ten sites in TD from 16 to 18 Oct 2013

From site 1 near the south edge of the Taklimakan Desert to site 10 at the north edge, Fig. 8 shows that the EOBS with wavelengths 8.3 m, 8.6 m and 9.1 m is higher over the oasis around TD than its hinterland. Starting from site 1, the CAMEL LSE first slowly decreases; reaching the minimum around site 7 at the hinterland of the Taklimakan Desert, then increases and finally reaches their maximum at site 10. This U shape is physically consistent with the geography of the region. At both the south and north ends of the ten sites, there are many oases where the soil is not sandy or not as sandy. So the LSE at both ends is larger than the sites in the inner desert. The CAMEL from the northern end is larger than the south end because site 10 is much closer to the oasis than site 1. Besides, site 10 has a clay ground surface while site 1 has a sandy surface. For the three long wavelength bands at 10.8 m, 11.3 m and 12.1 m, the CAMEL remains almost the same at all ten observing sites.

Since the EOBS covers 390 wavelengths, the 13-hinge point CAMEL ESDR database is expanded to 417 spectral channels (Fig. 9) using the software tool provided by the CAMEL team with a Principal Component (PC) regression approach (Borbas et al. 2018). While the 13 hinge points provide critical spectral information for the LSE, the high spectral resolution (HSR) CAMEL does provide more detailed spectral variations. At all ten sites, the HSR CAMEL clearly shows a spike around 8.6 m within the quartz reststrahlen band. Also, the dip starting around 12.3 m is also visible for all ten sites. The 13-hinge points, on the other hand, do not show such spectral signals. Therefore, the CAMEL HSR will also be used for inter-comparison with the measured LSE (EOBS).

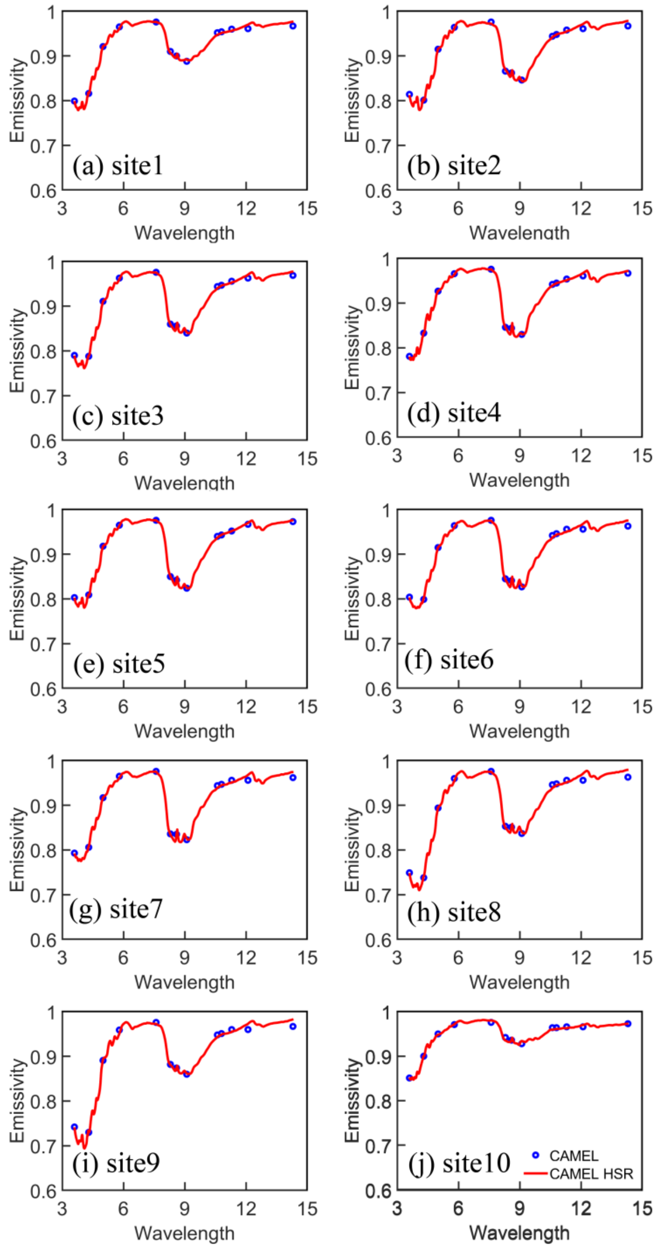

Fig. 9. CAMEL LSE expanded to high spectral resolution spectra from the CAMEL 13-hinge point emissivity value

3.3 Comparison between CAMEL and EOBS at hinge points in the quartz reststrahlen band

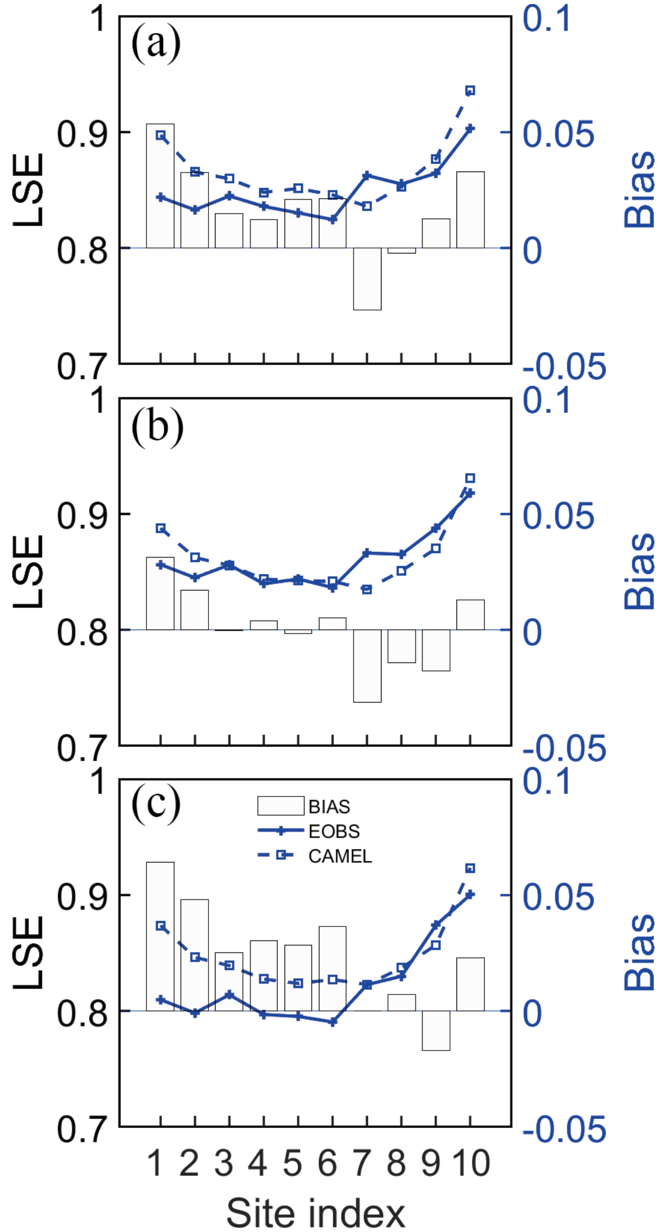

Fig. 10. CAMEL LSE (dashed line) and field measured LSE (EOBS, solid line) at (a) 8.3 m, (b) 8.6 m, (c) 9.1 m. The bars show the bias of CAMEL compared to EOBS (CAMEL minus EOBS

Fig. 10 shows the spatial variations of the CAMEL and the corresponding EOBS in the quartz reststrahlen band from sites 1 to 10. As pointed out before, the CAMEL shows a U-shaped spatial variation. CAMEL emissivity from site 1 is substantially larger than that from site 2. Both sites have LSE substantially larger than inner desert sites. However, the U shape from the EOBS is not as profound as from the CAMEL. EOBS at site 1 is only slightly larger than site 2. And neither is significantly larger than that from inner desert. For 8.3 m, CAMEL is greater than the corresponding EOBS for all sites except for site 7, as is showed in Fig 10(a). The largest discrepancy of 0.054 appeared at site 1. For LSE at 8.6 m, CAMEL is larger at sites 1, 2, and 10 and smaller at sites 7, 8, and 9. Other sites are similar. The maximum positive bias of 0.03 is at site 1, while maximum negative bias of -0.03 is at site 7. For 9.1 m, CAMEL is greater than EOBS for the first six sites while comparable for the last four sites. The Maximum positive bias of 0.06 again appeared at site 1. In addition, the averaged differences of CAMEL from EOBS (CAMEL minus EOBS) are around 0.017, 0.001, and 0.025 respectively for 8.3 m, 8.6 m, and 9.1 m. So overall, CAMEL emissivity is larger than the EOBS. The largest differences of LSE at all these three wavelengths appeared at site 1.

3.4 Comparison between HSR CAMEL and EOBS

Comparisons between EOBS and the corresponding HSR CAMEL (Fig. 11) offer an opportunity to examine the spectral differences in detail. The spectral variation of EOBS is similar to that of HSR CAMEL at all the ten observation sites. The quartz reststrahlen band is well recognized in both EOBS and CAMEL. The LSE in this quartz reststrahlen band is significantly smaller than those with wavelengths greater than 9.1 m. There are two spectral spikes in EOBS in the quartz reststrahlen band, one around 8.6 m and the other around 9.1 m. Both spikes are visible at most sites for EOBS, with the second spike not as profound. There are only one spike in CAMEL with its minimum at wavelength around 9 m approximately, which is somewhat different from that of EOBS. The LSE decreases around 12.3 m, and then increases around 12.8 m. This dip is well characterized by both. It is important to point out that these spectral spikes and dips are not artificially produced by the PCA noise filtering. They are also recognizable from the unfiltered data in Fig. 2. At site 8, the EOBS fits very well with HSR CAMEL, with their HSR curves almost overlapped with each other. This is consistent with the three hinge point comparison at this site shown in Fig. 10. The land-use category at this site is recognized as sheer sand and consistent with the actual situation observed during the field experiments.

Two possible reasons may contribute to the discrepancies between the CAMEL and EOBS. First, the CAMEL is an area measurement, while EOBS is a point measurement. CAMEL measurements are more affected by the oases nearby. The high LSE from the nearby oasis increases the CAMEL LSE significantly at site 1 and substantially at site 2. The EOBS at sites 1 and 2 were measured from the sand samples. So the large discrepancies at sites 1 and 2 are probably an indication that the two measurements are looking at different surface materials in the region. Secondly, the CAMEL is a monthly LSE database based on MODIS and ASTER on Terra, whose equator passing time is around 9:30 am and 9:30 pm approximately. So the CAMEL is the day/night average over one month. Li et al. (2012) showed that nighttime LSE is likely larger due to increased soil moisture from absorption [9]. The EOBS, on the other hand, is from daytime only, thus more likely smaller than the CAMEL.

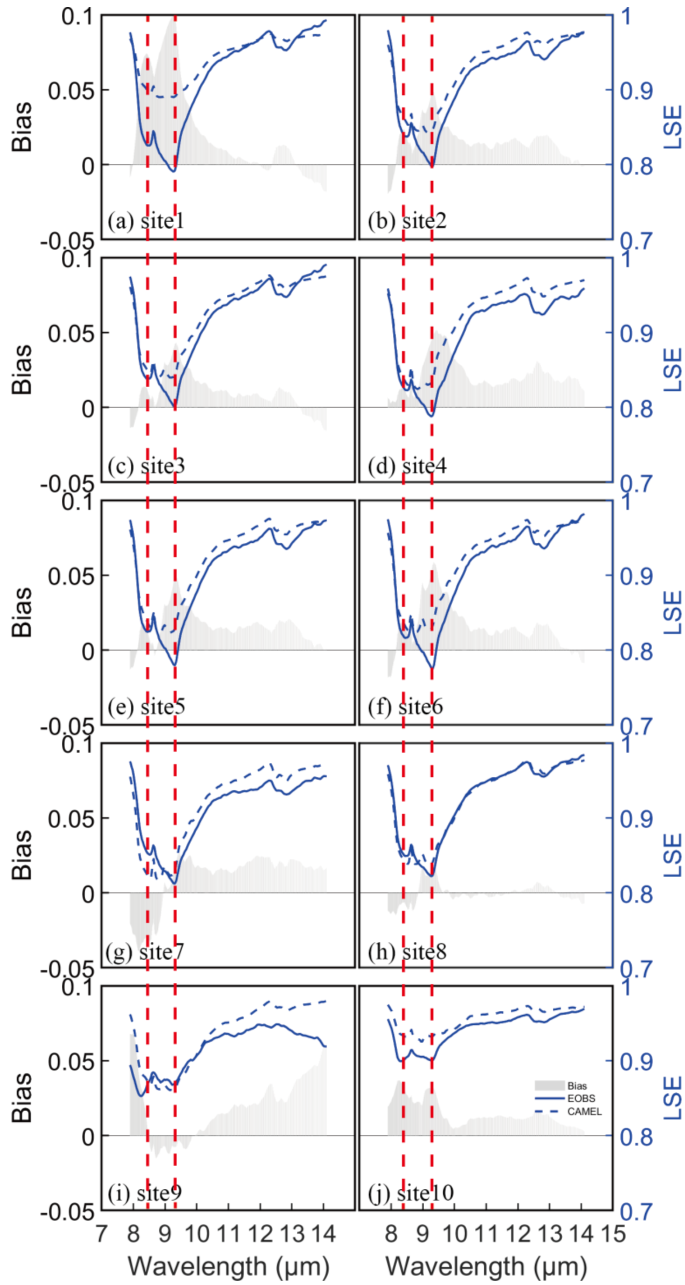

Fig. 11. The HSR CAMEL (dashed blue line) and EOBS (solid blue line) for the ten sites, as well as the bias (CAMLE minus EOBS, shaded column) between them. The EOBS has been filtered by using PCA. The CAMEL HSR is calculated from the emissivity values at 13-hinge points.

Comparisons between EOBS and the corresponding HSR CAMEL (Fig. 11) offer an opportunity to examine the spectral differences in detail. The spectral variation of EOBS is similar to that of HSR CAMEL at all the ten observation sites. The quartz reststrahlen band is well recognized in both EOBS and CAMEL. The LSE in this quartz reststrahlen band is significantly smaller than those with wavelengths greater than 9.1 m. There are two spectral spikes in EOBS in the quartz reststrahlen band, one around 8.6 m and the other around 9.1 m. Both spikes are visible at most sites for EOBS, with the second spike not as profound. There are only one spike in CAMEL with its minimum at wavelength around 9 m approximately, which is somewhat different from that of EOBS. The LSE decreases around 12.3 m, and then increases around 12.8 m. This dip is well characterized by both. It is important to point out that these spectral spikes and dips are not artificially produced by the PCA noise filtering. They are also recognizable from the unfiltered data in Fig. 2. At site 8, the EOBS fits very well with HSR CAMEL, with their HSR curves almost overlapped with each other. This is consistent with the three hinge point comparison at this site shown in Fig. 10. The land-use category at this site is recognized as sheer sand and consistent with the actual situation observed during the field experiments.

Two possible reasons may contribute to the discrepancies between the CAMEL and EOBS. First, the CAMEL is an area measurement, while EOBS is a point measurement. CAMEL measurements are more affected by the oases nearby. The high LSE from the nearby oasis increases the CAMEL LSE significantly at site 1 and substantially at site 2. The EOBS at sites 1 and 2 were measured from the sand samples. So the large discrepancies at sites 1 and 2 are probably an indication that the two measurements are looking at different surface materials in the region. Secondly, the CAMEL is a monthly LSE database based on MODIS and ASTER on Terra, whose equator passing time is around 9:30 am and 9:30 pm approximately. So the CAMEL is the day/night average over one month. Li et al. (2012) showed that nighttime LSE is likely larger due to increased soil moisture from absorption. The EOBS, on the other hand, is from daytime only, thus more likely smaller than the CAMEL.

Sites 2 – 8 are from the inner desert. There are smaller variations of emissivity between sites. The LSE diurnal variations due to soil moisture diurnal variations may cause EOBS smaller than CAMEL. Due to the lack of soil moisture observation during Oct 2013, 2-m relative humidity and surface skin temperature (Fig. 12) from site 5 are examined. Without the dominant factors affecting soil moisture from precipitation, irrigation, and groundwater, air humidity becomes the main factor affecting soil humidity through evaporation and adsorption. Small relative humidity and hot surface skin temperature both favor the evaporation and inhibit the moisture adsorption from the air to sand particles. Fig. 12 shows that the diurnal variation (maximum minus minimum) of 2-m relative humidity at site 5 can reach up to 57.0%. At the time EOBS were taken, the 2-m relative humidity was around 14.0%, which is much drier than the average value of 31.4%. Similarly, the surface skin temperature has a diurnal variation as large as 43.0 K. At the time EOBS were taken, the surface skin temperature was 25.8 K. Although this is not the hottest temperature of the day, it is much warmer than the monthly average of 14.2 K. It is therefore expected that the soil moisture at the time EOBS were taken be smaller than the monthly average from the CAMEL. And that is likely the main reason why the EOBS at sites 3-8 are mostly lower than the monthly averaged CAMEL.

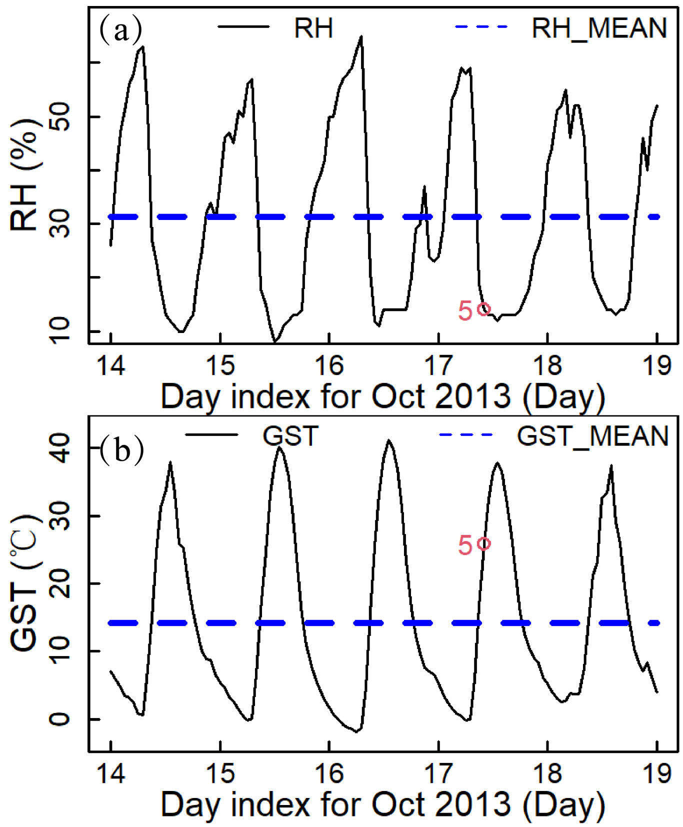

Fig. 12. (a) The 2-m relative humidity (RH) and (b) the ground surface skin temperature (GST) over site 5. The black curve stands for the hourly variation of 2-m RH and GST, blue dotted line for their mean, while the red circles denote the EOBS measurement time (local solar time) at site 5

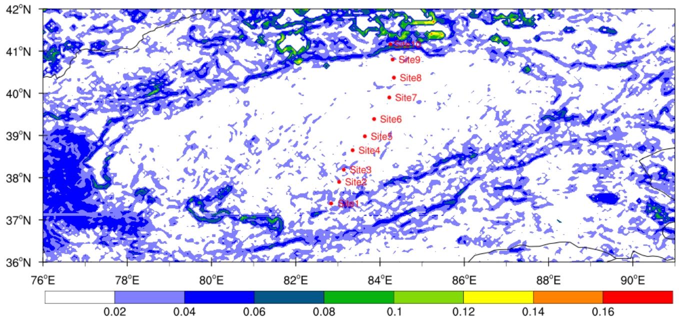

Fig. 13. The one-step spatial gradient (Unit: 1/5000m) of HSR CAMEL LSE over TD at 9.1 m

There are obvious differences between the EOBS and CAMEL. Emissivity in the quartz reststrahlen band has differences larger than 0.02. It has the largest differences at 9.1 m. The longer wavelengths between 11 m and 14 m have differences smaller than 0.02. As pointed out in the previous section, the differences can be caused by two possible reasons. To further illustrate that the CAMEL measurements at sites near southern and northern boundaries of the TD are strongly affected by nearby oases, Fig. 13 shows the spatial gradient of CAMEL emissivity at 9.1 m. Sites 1, 9, and 10 are located in or near areas with obvious spatial gradients. Both sites 1 and 10 have large spatial gradients. According to Liu et al. (2013), sites 1 has occasional vegetation cover of phragmite jeholensis and populus euphratica and sites 9 and 10 has occasional ramarix ramosissima and populus euphratica [30]. Thus the soil samples from these sites are not a good representative of the area. It may lead to smaller EOBS values than CAMEL.

4. DISCUSSION

Existing LSE databases are mostly monthly based and are from polar-orbiting satellites. The lack of temporal variations makes it difficult to use those LSE databases for satellite IR surface channel radiance assimilation over deserts. Geostationary imagers, such as the Advanced Geosynchronous Radiation Imager (AGRI), the Advanced Basline Imager (ABI), and the Spinning Enhanced Visible and InfRared Imager (SEVIRI), all have three longwave bands, one of which is in the quartz reststrahlen band. The high temporal resolution measurements from those imagers will provide useful information on the temporal variations of LSE in high spatial resolution. Geostationary hyperspectral IR sounders, such as the first GIIRS (spell out) on in-orbit Fengyun-4 satellites, the InfraRed Sounder (IRS) on to-be-launched Meteosat Third Generation (MTG), and the Geostationary and Extended Observations (GeoXO) Sounder (GXS) on the planned GeoXO, will have high spectral resolutions. Sounder measurements will complement the imager measurements with needed spectral information of LSE. Together, these geostationary sensors can be used to increase the temporal variations of the existing polar-orbiting satellite-based LSE database.

Existing monthly LSE database also does not account for angular variations, which have been discovered and demonstrated before [34, 35]. While no efforts have been made in this study to address this limitation, extensive LSE field measurements can be made to comprehensively understand how LSE changes with viewing angles over different desert surface types and in different weather conditions. Quantitatively understanding the angular and temporal variations of desert LSE can be used to develop an IR LSE model. An LSE database with adequate temporal and angular variations will make it possible to assimilate surface channel radiances, which contains important information for boundary layer. Note that there does not exist IR LSE models yet while IR emissivity models over ocean have been developed [36].

5. CONCLUSIONS

Ten sets of hyperspectral infrared (IR) land surface emissivity (LSE) spectra were obtained from field experiments on 16-18 Oct 2013. These were measured from 10 sites along a south/north desert road in TD. The original EOBS showed strong spectral noises, which were filtered out with a principal component analysis. The filtered field measured LSE is compared with CAMEL dataset from October 2013.

The CAMEL appears to capture the LSE spatial variations well over the TD. From site 1 at the south edge of the TD to site 10 at the north edge, CAMEL in the quartz reststrahlen band shows a U-shaped spatial variation, decreasing first, reaching their minimum at site 7, then increasing, and reaching their maximum at site 10. Sites near the desert edges have larger LSE due to the impact of nearby oases. Many of the surface features, such as water reservoirs, rivers, oases, and snow-covered mountain tops, are well characterized in the CAMEL LSE imagery. The CAMEL at 8.3 m shows zonal strips from northeast to southwest. Such artifacts are likely caused by the lack of temporal resolution from the ASTER LSE database.

The variation pattern from desert to oasis observed from the EOBS is not as profound as from CAMEL. Especially the spatial variation from site 1 to 3, the LSE decrease is not obvious from the EOBS. Comparing EOBS with the hyperspectral CAMEL shows differences larger than 0.02 for the quartz reststrahlen band and smaller than 0.02 for wavelengths from $10 - 14$ m. Two reasons may contribute to these differences. First, the CAMEL is an area measurement, while the EOBS is a point measurement. So CAMEL will have larger values where oases nearby, such as sites 1, 9, and 10. In addition, the CAMEL is a monthly averaged database, where day/night measurements from MODIS are both used. The EOBS, on the other hand, is measured in the daytime. The high surface skin temperature and low relative humidity in the daytime favor evaporation and inhibit the moisture adsorption from air to sand particles. This may lead to lower measured EOBS than the CAMEL. This is consistent with previous studies where LSE diurnal variations were reported as a result of soil moisture diurnal variations.

These results indicate that the LSE in TD has strong spatial variations, especially near the desert edge. In the inner desert, the LSE spatial variations are not as strong. However, both desert edge and inner desert may be subject to LSE diurnal variations when soil moisture varies diurnally. For example, strong solar heating during the day may significantly increase the surface skin temperature and decrease 2-m relative humidity in the daytime. The soil moisture loss, as a result, leads to reduced LSE.

APPENDIX

Fig. A1. The measurement equipment FTIR used in the field observation experiments.

TABLE A . SURFACE LABEL INDICES AND THEIR CORRESPONDING LAND TYPE DESCRIPTION

Label	land cover description
0	No Data
10	Cropland, rainfed
20	Cropland, irrigated or post-flooding
30	Mosaic cropland (>50%) / natural vegetation (tree, shrub, herbaceous cover) (<50%)
40	Mosaic natural vegetation (tree, shrub, herbaceous cover) (>50%) / cropland(<50%)
50	Tree cover, broad-leaved, evergreen, closed to open (>15%)
60	Tree cover, broad-leaved, deciduous, closed to open (>15%)
70	Tree cover, needle-leaved, evergreen, closed to open (>15%)
80	Tree cover, needle-leaved, deciduous, closed to open (>15%)
90	Tree cover, mixed leaf type (broad-leaved and needle-leaved)
100	Mosaic tree and shrub (>50%) / herbaceous cover (<50%)
110	Mosaic herbaceous cover (>50%) / tree and shrub (<50%)
120	Shrubland
130	Grassland

Label	land cover description
140	Lichens and mosses
150	Sparse vegetation (tree, shrub, herbaceous cover) (<15%)
160	Tree cover, flooded, fresh or brackish water
170	Tree cover, flooded, saline water
180	Shrub or herbaceous cover, flooded, fresh/saline/brackish water
190	Urban areas
200	Bare areas
201	Consoildated bare areas
202	Unconsoildated bare areas
210	Water bodies
220	Permanent snow and ice

TABLE A LABORATORY MEASURED SOIL MATERIAL LIST

Index	Material list
1	leaf of twig
2	Sliced santa barbara sand stone
3	Flat rwer washed stone
4	Soil(Oklahoma),1st meas. on 11/07/96 (wet sample)
5	Soil(Oklahoma),2nd meas. on 11/27/96 (dry)
6	Soil(Oklahoma),3rd meas. on 12/04/96 (more dry)
7	Soil(Oklahoma),4th meas. on 01/27/97 (very dry)
8	Sample of surface in Death Valley
9	Sample of surface in Death Valley
10	Sample of surface in Death Valley
11	Sample of surface in Death Valley
12	Sample of surface in Death Valley
13	Sample of surface in Death Valley
14	Soil 88p2535S from Nebraska Soil Lab
15	Soil Sample of Haliia from Nebraska Soil Lab
16	Soil 88p2535S from Nebraska Soil Lab
17	Soil 88p3715S from Nebraska Soil Lab
18	Soil 88p4643S from Nebraska Soil Lab
19	Soil 90p3101S from Nebraska Soil Lab
20	Soil 90P3921S from Nebraska Soil Lab
21	Soil 90P4172S from Nebraska Soil Lab
22	Soil 90P4255S from Nebraska Soil Lab
23	Soil 90P_476S from Nebraska Soil Lab
24	Leaf of Algerian Ivy (Hedera Canariensis Algerian Ivy)
25	Leaf of Arailia japonica
26	Leaf of Bird of Paradise (Strelitzea/Nicolai)
27	Leaf of Bronze Loquat (eriobotrya)
28	Leaf of Brazilian Peppertree (schinus terebinthifdias)

Index	Material list
29	Clay Brick (Common)
30	Soil Sample 1 from Concord, MA
31	Soil Sample 2 from Concord, MA
32	Soil Sample 3 from Concord, MA
33	Leaf of Cypress
34	Soil Sample 1 from Death Valley, CA
35	Soil Sample 2 from Death Valley, CA
36	Soil Sample 3 from Death Valley, CA
37	Soil Sample 4 from Death Valley, CA
38	Soil Sample 5 from Death Valley, CA
39	Soil Sample 6 from Death Valley, CA
40	Soil Sample 7 from Death Valley, CA
41	Soil Sample 8 from Death Valley, CA
42	Soil Sample 9 from Death Valley, CA
43	Soil Sample 10 from Death Valley, CA
44	Douglas Fir
45	Emissivity of Dry Grass (Averaged over 9 Sets)
46	Emissivity of Dry Grass (Averaged over 9 Sets)
47	Emissivity of Dry Grass (Averaged over 9 Sets)
48	Sample of surface in Death Valley
49	Sample of surface in Death Valley
50	Sample of surface in Death Valley
51	Sample of surface in Death Valley
52	Sample of surface in Death Valley
53	Fresh leaf of Eucalyptus tree
54	Leaf of Eucalyptus tree
55	Leaf of Evergreen Pear (pyrus Kawakami evergreen pear)
56	Flat River Washed Stone
57	Sand Sample 1 - Goleta Beach (Goleta, CA)
58	Sand Sample 2 - Goleta Beach (Goleta, CA)
59	Leaf of Green Spruce from Canada
60	Sample 1 - Emissivity of Smooth Ice (Mammoth Lakes)
61	Sample 2 - Emissivity of Smooth Ice (Mammoth Lakes)
62	Sample 3 - Emissivity of Smooth Ice (Mammoth Lakes)
63	Leaf of India Hawthorne (Raphiolepis India)
64	Sample 1 of Surface in Koehn, CA
65	Sample 2 of Surface in Koehn, CA
66	Sample 4 of Surface in Koehn, CA
67	Sample 5 of Surface in Koehn, CA
68	Sample 6 of Surface in Koehn, CA
69	Leaf of Laurel Tree (ficus microcarpa nitida)
70	Laurel leaf
71	Leaf of Laurel (Fresh)
72	Leaf Magnolia (1st day)

Index	Material list
73	Leaf of Maple (Red Star)
74	Leaf of Myoporum (myoporum laetum)
75	Leaf of Naked Coral Tree (Erythrina coraloides)
76	Leaf of Oak (Face)
77	oil Sample 1 from Oklahoma
78	Soil Sample 2 from Oklahoma
79	Soil Sample 3 from Oklahoma
80	Soil Sample 4 from Oklahoma
81	Soil Sample 5 from Oklahoma
82	Soil Sample 6 from Oklahoma
83	Soil Sample 7 from Oklahoma
84	Soil Sample 8 from Oklahoma
85	Soil Sample 9 from Oklahoma
86	Soil Sample 10 from Oklahoma
87	Soil Sample 11 from Oklahoma
88	Soil Sample 12 from Oklahoma
89	Soil Sample 13 from Oklahoma
90	Soil Sample 14444 from Oklahoma
91	Leaf of Pine (New)
92	Leaf of Pine (Old)
93	Sample 1 of Surface from Railroad Valley - Playa
94	Sample 2 of Surface from Railroad Valley - Playa
95	Sample 3 of Surface from Railroad Valley - Playa
96	Sample 4 of Surface from Railroad Valley - Playa
97	Sample 5 of Surface from Railroad Valley - Playa
98	Sample 6 of Surface from Railroad Valley - Playa
99	Sample 7 of Surface from Railroad Valley - Playa
100	Sample 8 of Surface from Railroad Valley - Playa
101	Sample 9 of Surface from Railroad Valley - Playa
102	Sample 10 of Surface from Railroad Valley - Playa
103	Powder Sample 1 from Railroad Valley
104	Powder Sample 2 from Railroad Valley
105	Seawater - Emissivity Averaged Over 18 Sets (Goleta)
106	Seawater - Emissivity Averaged Over 18 sets (Goleta)
107	Seawater - Emissivity Averaged Over 10 sets
108	Leaf of Shiny Xylosma (xylosma corgostum)
109	Sliced Santa Barbara Sandstone
110	Emissivity of Salty Soil (Averaged over 9 Sets)
111	Soil Sample 1 (Page, Arizona)
112	Soil Sample 2 (Page, Arizona)
113	Soil Sample 3 (Page, Arizona)
114	Soil Sample 4 (Page, Arizona)
115	Soil Sample 5 - Non Productive Vegetation (Page, Arizona)
116	Soil Sample 6 (Page, Arizona)

Index	Material list
117	Soil Sample 7 - Hard Pan, Fractured Somewhat (Page, Arizona)
118	Soil Sample 8 - Hard Pan, Ground (Page, Arizona)
119	Soil Sample 9 - Hard Pan, Ground (Page, Arizona)
120	Sample 1 - Emissivity of Ice Snow - Average of 3 Sets (Mammoth Lakes)
121	Sample 2 - Emissivity of Ice Snow (Mammoth Lakes)
122	Leaf of Sweet Gum (liquidamber styreciflua)
123	Leaf of Tasmanian Bluegum Eucalyptus (Eucalyptus Globulus)

* The shaded rows indicate the selected 42 desert-related sample

Funding: This research was funded by the Central Scientific Research Institute of the Public Basic Scientific Research Business Professional (IDM2021003, IDM2021001) and the National Natural Science Foundation of China (41875023)

Acknowledgments: The authors thanks to Professor Yongqiang Liu in College of Resource and Environmental Sciences, Xinjiang University, Urumqi, China for conduction of the EOBS field experiments.

Conflicts of Interest: The authors declare no conflict of interest.

References

1. LV X, Zhou Y, and Yu X, "Temporal and spatial variation characteristics of rainstorm and mountain torrential flood disaster loss in Xinjiang from 1961 to 2019," *Dese. Oas. Meteo.* vol. 15, pp. 42-49, 2021. doi: 10.12057/j.issn.1002-0799.2021.04.006

2. Bauer P, Thorpe A and Brunet G, "The quiet revolution of numerical weather prediction," *Nature.* vol. 525, pp. 47-55, 2015. doi: 10.1038/nature14956.

3. Yan J H and Majewski D, "Experimental study of the role of initial and boundary conditions in mesoscale numerical weather prediction," *J. TROP. METEOROL.* vol. 9, pp. 134-142. , 2003. doi: 10.3969/j.issn.1006-8775.2003.02.003

4. Yufen Ma, Ali Mamtimi and, Guangxing Zhang, "Observation en-or diagnostics and applicability evaluation of MHS brightness temperatures in RMAPS-CA," *Int. J. Remote. Sens.* vol. 42, pp. 5626-5647., 2021. doi: 10.1080/01431161.2021.1929544

5. Eyre J R, English S J and Forsythe M, "Assimilation of satellite data in numerical weather prediction. Part I: The early years," *Q. J. R. Meteorol. Soc.* vol. 146, pp. 49-68. , 2019. doi: 10.1002/qj.3654

6. Yin R, Han W, Gao Z and Di D, "The evaluation of FY4As Geostationary Interferometric Infrared Sounder (GIIRS) long-wave temperature sound-

ing channels using the GRAPES global 4D-Var," *Q. J. R. Meteorol. Soc.* vol. 146, pp. 1459–1476. , 2020. doi: 10.1002/qj.3746

7. Xue Jishan, "Scientific issues and perspective of assimilation of meteorological satellite data," *Acta. Sinica.* 2009, vol. 67, pp. 903-911. , doi: 10.3321/j.issn:0577-6619.2009.06.001

8. Mc Nally, A. P., P. D. Watts, J. A. Smith, R. Engelen, G. A. Kelly, J. N. Thepaut, and M. Matricardi, "The assimilation of AIRS radiance data at ECMWF," *Q. J. R. Meteorol. Soc.* vol. 132, pp. 935–957. , 2006. doi: 10.1256/qj.04.171

9. Li, Z., J. Li, Y. Li and WP Menzel, "Determining diurnal variations of land surface emissivity from geostationary satellites," *J. Geophys. Res.* vol. 117, pp. D23302. , 2012,doi: 10.1029/2012JD018279

10. Pavelin E G and Candy B, "Assimilation of surface-sensitive infrared radiances over land: Estimation of land surface temperature and emissivity. *Q. J. R. Meteorol. Soc.* vol. 140. , 2014. doi: 10.1029/2012JD018279

11. Han W. and Mc Nally AP, "The 4D-Var assimilation of ozone-sensitive infrared radiances measured by IASI," *Q. J. R. Meteorol. Soc*, vol. 136, pp. 2025–2037, 2010. doi: 10.1002/qj.708

12. D Di, Li, J. , Han, W. , Bai, W. , Wu, C. and Menzel, W. P, "Enhancing the fast radiative transfer model for Feng Yun- 4 GIIRS by using local training profiles," *J Geophy Res: Atmospheres*, vol. 123(22) , pp. 12583-12596. , 2018. doi: 10.1029/2018JD029089

13. Li, Z., J. Li, X. Jin, T. J. Schmit, E. E. Borbas and M. D. Goldberg, "An objective methodology for infrared land surface emissivity evaluation," *J. Geophys. Res.* vol. 115, pp. D22308. , 2010. doi: 10.1029/2010JD014249

14. Lin, P.-L., Chen, Y.-L., Chen, C.-S., Liu, C.-L. and Chen, C.-Y, "Numerical experiments investigating the orographic effects on a heavy rainfall event over the northwestern coast of Taiwan during TAMEX IOP 13," Meteorol. *Atmospheric Phys.* 2011, vol. 114, pp. 35–50. , 2011. doi: 10.1007/s00703-011-0155-7

15. Yang, K., T. Watanabe, T. Koike, X. Li, H. Fujii, K. Tamagawa, Y. Ma and H. Ishikawa, "Auto-calibration System Developed to Assimilate AMSR-E Data into a Land Surface Model for Estimating Soil Moisture and the Surface Energy Budget," *J. Meteorol. Soc. Japan.* vol. 85A, pp. 229–242. , 2007. doi: 10.2151/jmsj.85A.229

16. Jiménez-Muñoz, J.C., Sobrino, J.A., Gillespie, A., Sabol, D. and Gustafson, W.T, "Improved land surface emissivities over agricultural areas using ASTER NDVI," *Remote Sens. Environ.* 2006, vol. 103, 474–487. , doi: 10.1016/j.rse.2006.04.012

17. Stathopoulou, M., Cartalis, C. and Petrakis, M, "Integrating Corine Land Cover data and Landsat TM for surface emissivity definition: Application to the urban area of Athens, Greece," *Int. J. Remote Sens.* vol. 28, pp. 3291–3304. , 2007. doi: 10.1080/01431160600993421

18. Dee, D.P., Uppala, S.M., Simmons, A.J., Berrisford, P., Poli, P., Kobayashi, S., Andrae, U., Balmaseda, M.A., Balsamo, G., and Bauer, P., "The ERA-Interim reanalysis: Configuration and performance of the data assimilation system," *Q. J. R. Meteorol. Soc.* vol. 137, pp. 553–597. , 2011. doi: 10.1002/qj.828

19. Hulley, G., Veraverbeke, S. and Hook, S, "Thermal-based techniques for land cover change detection using a new dynamic MODIS multispectral emissivity product (MOD21) ," *Remote Sens. Environ.* vol. 140, pp. 755–765. , 2014. doi: 10.1016/j.rse.2013.10.014

20. Zhang, R., Kim, S. and Sharma, A, "A comprehensive validation of the SMAP Enhanced Level-3 Soil Moisture product using ground measurements over varied climates and landscapes," *Remote Sens. Environ.* vol. 223, pp. 82–94. , 2019, doi: 10.1016/j.rse.2019.01.015

21. Hulley, G. and Hook, S, "MOD21 MODIS/Terra Land Surface Temperature/3-Band Emissivity 5-Min L2 1 km V006, NASA EOSDIS Land Processes DAAC: Sioux Falls," *SD*, USA, vol. 2017, doi: 10.21029/22009JD012038

22. Hulley, G.C. and Hook, S.J, "Generating Consistent Land Surface Temperature and Emissivity Products Between ASTER and MODIS Data for Earth Science Research," *IEEE Geosci. Remote Sens. Lett.* , vol. pp. 1304–1315. , 2010, doi: 10.1109/TGRS.2010.2063034.

23. Vogel, R., Liu, Q., Han, Y. and Weng, F, "Evaluating a satellite-derived global infrared land surface emissivity data set for use in radiative transfer modeling," *J. Geophys. Res. Atmos.* 2011, vol. 116, pp. 11. , doi: 10.1029/2010jd014679

24. Borbas, E., Glynn, H. , Michelle, F. , "Robert, K. and Simon, H. The Combined ASTER MODIS Emissivity over Land (CAMEL) Part 1: Methodology and High Spectral Resolution Application," *Remote. Sens.* vol. 10, pp. 643. , 2018,doi: 10.3390/rs10040643

25. Li, Z., J. Li, Y. Li, Y. Zhang, T. J. Schmit, L. Zhou, M. D. Goldberg, and W. P. Menzel, "Determining diurnal variations of land surface emissivity from geostationary satellites," *J. Geophys. Res.* vol. 117, pp. D23302, 2012, doi: 10.1029/2012jd018279

26. Wan Zhengming and Zhao-Liang, "A physics-based algorithm for retrieving land-surface emissivity and temperature from EOS/MODIS data. *IEEE Geosci*," *Remote. Sens. Lett.* vol. 35, pp. 980-980. , 1997, doi: 10.1109/36.602541

27. Suzanne W. Seemann, Eva E. Borbas, Robert O. Knuteson Gordon R. Stephenson and Hung-Lung Huang, "Development of a global infrared land surface emissivity database for application to clear sky s.ounding retrievals from multispectral satellite radiance measurements," *J. Appl. Meteorol. Clim.* vol. 47, pp. 108-123, 2008, doi: 10.1175/2007JAMC1590.1.

28. Hulley, G. C., Hook, S. J., Abbott, E., Malakar, N., Islam, T. and Abrams, M, "The ASTER Global Emissivity Dataset (ASTER GED): Mapping Earths emissivity at 100 meter spatial scale," *Geophys. Res. Lett.* vol. 42, pp. 7966-7976. , 2015, doi: 10.1002/2015GL065564

29. Michelle, F. , Eva, B. , Robert, K. , Glynn, H. and Simon, H. "The Combined ASTER MODIS Emissivity over Land (CAMEL) Part 2: Uncertainty and Validation," *Remote Sensing*, vol. 10(5) , pp. 664. 2018a , doi: 10.3390/rs10050664

30. Liu Y., Ali Mamtimin, Huo W, Yang X, Liu Xn and He Q, "The characteristics of surface emission rate and distribution change in Taklamakan Deser," *Desert and Oasis Meteorology*, vol. 8(3) , pp. 1-7. 201, 2014,doi 10.3969/j.issn.1002-0799.2014.03.001

31. Korb A R, Dybwad P, Wadsworth W and Salisbury, J. W. , "Portable Fourier transform infrared spectrometer for field measurements of radiance and emissivity," *Applied Optics*, 35(10) , pp. 1679-1692. , 1996,doi: 10.1364/AO.35.001679

32. Andrew, et al, "Thermal-infrared remote sensing and Kirchhoff s law: 2. Field measurements," *Journal of Geophysical Research: Solid Earth*, vol. 104(B7) , pp. 15339-15350. , 1999, doi: 10.1029/97jb03537

33. Baldridge, A.M., Hook, S.J., Grove, C.I. and Rivera, G, "The ASTER Spectral Library Version 2.0," *Remote Sens.*Environ. vol. 114, pp. 711–715. , 2009,doi: 10.1016/j.rse.2008.11.007.

34. Francois, C., C. Ottlé, and L. Prevot, "Analytical parameterization of canopy directional emissivity and directional radiance in the thermal infrared. Application on the retrieval of soil and foliage temperatures using two directional measurements", *Int. J. Remote Sens.,* vol. 18, pp. 2587–2621, 1997, doi:10.1080/014311697217495.

35. Mc Atee, B., A. F. Prata, and M.-J. Lynch, "The behavior of emitted thermal infrared radiation (8–12 mm) at a semiarid site", *J. Appl. Meteorol.*, vol. 42, pp. 1060–1071, 2003, doi:10.1175/1520-0450.

36. Jun Yang and Qilong Min, "A passive and active microwave-vector radiative transfer (PAM-VRT) model". *J Quant Spectrosc RA.* vol. 165, pp. 123-133, 2015 https://doi.org/10.1016/j.jqsrt.2015.06.028.